

Super-Resolution Multi-Contrast Unbiased Eye Atlases With Deep Probabilistic Refinement

Ho Hin Lee*, Adam M. Saunders*, *Graduate Student Member, IEEE*, Michael E. Kim, Samuel W. Remedios, Yucheng Tang, *Graduate Student Member, IEEE*, Qi Yang, Xin Yu, Shunxing Bao, Chloe Cho, Louise A. Mawn, Tonia S. Rex, Kevin L. Schey, Blake E. Dewey, Jeffrey M. Spraggins, Jerry L. Prince, *Life Fellow, IEEE*, Yuankai Huo, *Senior Member, IEEE*, Bennett A. Landman, *Senior Member, IEEE*

Abstract—Eye morphology varies significantly across the population, especially for the orbit and optic nerve. These variations limit the feasibility and robustness of generalizing population-wise features of eye organs to an unbiased spatial reference. To tackle these limitations, we propose a process for creating high-resolution unbiased eye atlases. First, to restore spatial details from scans with a low through-plane resolution compared to a high in-plane resolution, we apply a deep learning-based super-resolution algorithm. Then, we generate an initial unbiased reference with an iterative metric-based registration using a small portion of subject scans. We register the remaining scans to this template and refine the template using an unsupervised deep probabilistic approach that generates a more expansive deformation field to enhance the organ boundary alignment. We demonstrate this framework using magnetic resonance images across four different MRI tissue contrasts, generating four atlases in separate spatial alignments. For each tissue contrast, we find a significant improvement in the average Dice score across four labeled regions compared to a standard registration framework consisting of rigid, affine, and deformable transformations. These results highlight the effective alignment of eye organs and boundaries using our proposed process. By combining super-resolution preprocessing and deep probabilistic models, we address the challenge of generating an eye atlas to serve as a standardized reference across a largely variable population.

Index Terms—Deep learning, medical image registration, multi-contrast imaging, unbiased eye atlas, super-resolution

This research is supported by the NIH Common Fund U54 DK134302 and U54 EY032442 (Spraggins), NSF CAREER 1452485, NIH 2R01EB006136, NIH 1R01EB017230, NIH R01DK13557, and NIH RO1NS09529. ImageVU and RD are supported by the VICTR CTSA award (ULTR000445 from NCATS/NIH). We gratefully acknowledge the support of NVIDIA Corporation with the donation of the Titan X Pascal GPU usage. This work involved de-identified data obtained from human subjects. Approval was granted by the Institutional Review Board (IRB 131461). This paper was presented in part at the SPIE Medical Imaging Conference, San Diego, CA, February 2023. (*Ho Hin Lee and Adam M. Saunders contributed equally to this work. Corresponding author: Adam M. Saunders, email: adam.m.saunders@vanderbilt.edu.)

Ho Hin Lee, Michael E. Kim, Qi Yang, Xin Yu, and Yuankai Huo are with the Department of Computer Science, Vanderbilt University, Nashville, TN 37235 USA.

Adam M. Saunders, Yucheng Tang, Shunxing Bao, and Bennett A. Landman are with the Department of Electrical and Computer Engineering, Vanderbilt University, Nashville, TN 37235 USA.

I. INTRODUCTION

Significant variation in human eye morphology, especially in the shape and size of the orbit and the optic nerve sheath diameter (ONSD), presents challenges in medical imaging to generalize population-wise features of eye organs to a spatial reference image. Different volumetric imaging modalities capture distinct perspectives on eye morphology. Typical imaging modalities include computed tomography (CT), magnetic resonance imaging (MRI), ultrasonography, and optical coherence tomography (OCT). The diversity of imaging protocols increases the amount of contextual information available. For example, researchers have used OCT to create a reproducible measure of the curvature of the eye [1]. Contrast agents injected into the vascular system can highlight abnormal tissues like lesions and tumors. In MRI, different imaging sequences result in different relaxation weightings, producing distinct tissue contrasts.

Even in healthy individuals, there is significant variation in orbit and optic nerve morphology. Differences in eye morphology have been associated with demographic variables like sex and ethnicity [2]. Researchers have used CT scans to find associations between orbital skull landmarks and sex and ethnicity [3], [4]. A study examining ONSD in 585 healthy adults using ultrasonography found that the ONSD ranged from 3.30 mm to 5.20 mm and eyeball transverse diameter (ETD) ranged from 20.90 mm to 25.70 mm [5]. Similarly, another study with 300 healthy participants found that the ONSD diameter ranged from $5.17 \text{ mm} \pm 1.34 \text{ mm}$ to 3.55 mm

Samuel W. Remedios is with the Department of Computer Science, Johns Hopkins University, Baltimore, MD 21218 USA.

Chloe Cho is with the Department of Biomedical Engineering, Vanderbilt University, Nashville, TN 37235 USA.

Louise A. Mawn and Tonia S. Rex are with the Department of Ophthalmology and Visual Sciences, Vanderbilt University Medical Center, Nashville, TN 37232 USA.

Kevin L. Schey is with the Department of Biochemistry, Vanderbilt University, Nashville, TN 37240 USA.

Blake E. Dewey and Jerry L. Prince are with the Department of Electrical and Computer Engineering, Johns Hopkins University, Baltimore, MD 21218 USA.

Jeffrey M. Spraggins is with the Department of Cell and Developmental Biology, Vanderbilt University, Nashville, TN 37253 USA.

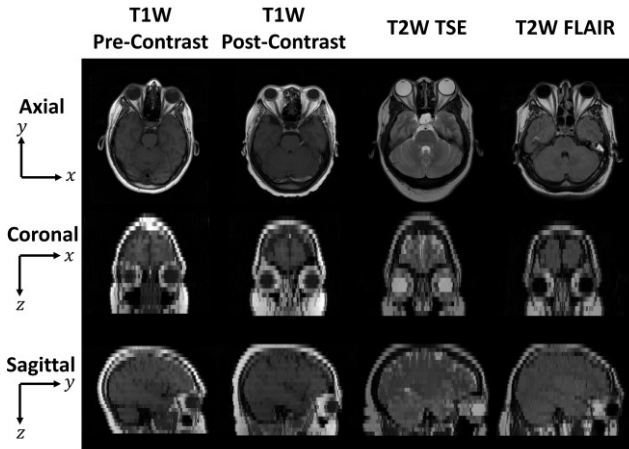


Fig. 1. Representative in-plane (axial, first row) and through-plane (coronal, second row and sagittal, third row) slices for four MRI tissue contrasts from four different subjects. The coronal and sagittal through-plane slices are lower resolution than the axial in-plane slices and are visualized with nearest neighbor interpolation. The relatively lower resolution limits our ability to distinguish organs and generalize anatomical characteristics across populations.

± 0.82 mm at different locations in the intra-orbital space using CT imaging [6]. In addition, variation in eye morphology, particularly in the globe, depends on conditions that affect visual acuity, such as myopia and hyperopia. Researchers have used MRI to associate myopia with posterior eye shape [2]. A study examining differences in eye shape on MRI in emmetropia and myopia found that the globe is larger in all dimensions (with the largest changes axially followed by vertically then horizontally) as myopic refractive correction increases. Specifically, in myopia, the globe dimensions ranged from 22.1 mm to 27.3 mm axially, 21.1 mm to 25.9 mm vertically, and 20.8 mm to 26.1 mm horizontally. Even the typical emmetropic eye contains substantial variation across a population [7], [8]. These variations highlight the difficulty in creating a standardized reference image that is not biased by known differences in eye morphology.

Atlases are standardized reference images that are useful for tasks such as image registration and cross-sectional comparisons. For atlases to be representative of a population, it is important that they not be biased toward the morphology, contrast levels, or health conditions of any subject used in their creation. Given the variation across a population, it is challenging to generalize the population characteristics of both eye morphology and contrast intensity in a single anatomical reference template to define the conditional characteristics of the organ-specific regions (e.g., healthy or diseased). To enhance the generalization of eye organ contexts from different imaging protocols, we investigate the contextual variability in different tissue contrasts in MRI. Volumetric scans often have a lower resolution in the through-plane (x - z or coronal plane and y - z or sagittal plane) than that of the in-plane (x - y or axial plane), where the x -axis is the left/right axis, the y -axis is the anterior/posterior axis, and the

z -axis is the superior/inferior axis (Fig. 1). The low-resolution characteristics in the through-plane limit context for aligning the eye anatomies. Previous works have demonstrated the feasibility of leveraging deep learning super-resolution algorithms to restore the image quality [9]. Consequently, we explore two questions:

- 1) Can we further apply a deep super-resolution algorithm to multiple MRI tissue contrasts?
- 2) Can we leverage the super-resolution imaging to generate refined unbiased eye atlas templates?

In this work, we propose a coarse-to-fine framework to enhance the image resolution and leverage the restored details to generate a refined unbiased eye atlas specific to several tissue contrasts. We generate a separate atlas for each tissue contrast, so the atlases are not in spatial alignment. The complete backbone consists of three steps: 1) applying a deep super-resolution network to enhance through-plane resolution quality; 2) generating an efficient coarse unbiased template from a small population of samples; and 3) refining the template by applying a deep probabilistic network for large population samples. The experimental results show that the application of the super-resolution network enhances the appearance of the eye organ. With the probabilistic refinement, our method achieves state-of-the-art registration performance when compared to deep learning registration baselines across all datasets. Our contributions are summarized here:

- 1) We propose a two-stage framework to enhance the through-plane resolution of imaging across different tissue contrasts and adapt the restored high-resolution context for eye atlas generation.
- 2) We propose a coarse-to-fine registration strategy that combines both metric-based and deep learning-based registration to perform across large population samples.
- 3) We evaluate our generated atlas with inverse eye organ label transfer from atlas space to moving subject space, demonstrating significant improvements in the Dice score across all tissue contrasts.
- 4) All generated atlases as well as the corresponding four eye organ labels will be used through the Human BioMolecular Atlas Program (HuBMAP) [10].

II. RELATED WORKS

A. Atlas Generation

Significant efforts have been dedicated to exploring biomarkers with brain MRI using other frameworks [11], [12]. Kova et al. recognized the similarities between the human and mouse brains and proposed a 3D variational mouse brain atlas to represent populational anatomy and variations [13]. Wang et al. use 1675 specimens of mouse brain MRI to generate an average mapping framework [14]. In a different approach, Shi et al. developed an unbiased infant brain atlas registration of MRI scans from 56 males and 39 females, encompassing three different scanning time points. They applied groupwise

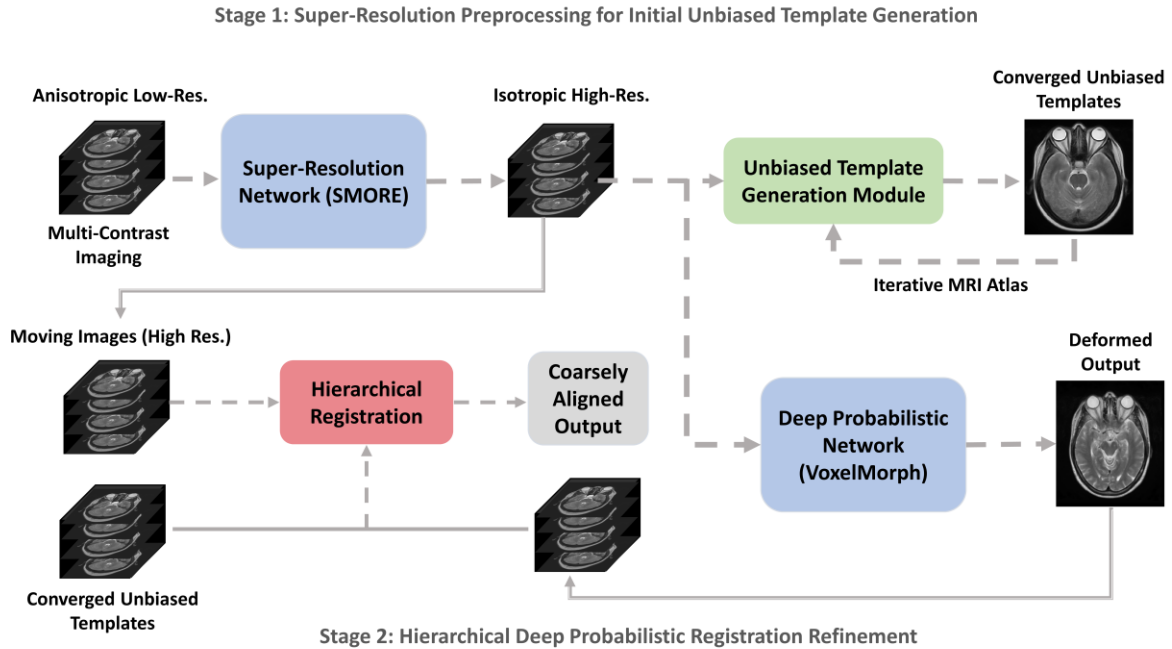


Fig. 2. The complete pipeline for unbiased eye atlas generation consists of two stages: 1) performing a deep learning super-resolution algorithm to enhance image quality and distinguish organ appearances and 2) combining metric-based and deep learning-based registration through a hierarchical registration framework for refined anatomical transfer.

registration to avoid biasing the atlas to a single target image for registration [15]. Kuklisova-Murgasova et al. introduced multiple atlases to capture the aging characteristics of infants between 29 and 44 weeks [16]. Ali et al. generated an unbiased spatial-temporal 4-D atlas and a time-variable longitudinal atlas for infant brains, using symmetric diffeomorphic deformable registration to avoid bias [17]. To investigate the aging characteristics in brain tissue, Yuyao et al. utilized patch-based registration in the spatial-temporal wavelet domain to generate a longitudinal atlas [18]. While previous efforts primarily focused on creating healthy brain atlas templates, Rajashekar et al. proposed high-resolution normative atlases for visualizing population-wise representations of brain diseases, including brain lesion and stroke using fluid-attenuated inversion recovery (FLAIR) MRI and non-contrast CT modalities [19]. Abdominal studies have developed a multi-contrast kidney atlas, incorporating both contrast and morphological characteristics within kidney organs [20], [21]. Researchers have extended kidney atlas templates to encompass substructure organs, such as the medulla, renal cortex, and pelvicalyceal systems in kidney regions using arterial phase CT [22]. However, limited research has addressed the creation of a standard reference atlas for the eye, which presents challenges due to its complex morphology and the influence of conditions that affect the eye shape, e.g., myopia and hyperopia.

B. Medical Image Registration

To accurately transfer the varied anatomical context from the moving subject to the atlas target, the image registration algorithm must be robust. One straightforward approach to enhancing registration performance is to adapt both affine and

deformable transformations hierarchically with metric-guided optimization [23]–[25]. Furthermore, spatial optimization approaches attempt to regularize the deformation field to effectively align the anatomical context (e.g., discrete optimization [26], b-spline deformation [27], Demons [28], and symmetric normalization [24]). However, the computational efficiency of these spatial transformations is limited.

Registration algorithms with deep neural networks aim to enhance both computational efficiency and robustness in an unsupervised setting. VoxelMorph is a foundational network that adapts a large deformation field to align the significant variation across anatomies [25], [29]. Researchers have also adapted VoxelMorph to produce diffeomorphic deformations, i.e., deformations that are smooth and invertible [29]. To differentiate the two networks, we refer to the former as VoxelMorph-Original and the latter as VoxelMorph-Probabilistic. Zhao et al. crop the organ regions of interest (ROIs) and recursively register the anatomical context with VoxelMorph-Original [30], while Yang et al. predict a bounding box to first localize the organ ROIs and perform registration [31]. Although deep learning-based approaches demonstrate their effectiveness to enhance the computational efficiency of registration algorithms, instability with the registration performance may arise due to substantial domain shifts with unseen data [21].

III. METHODS

Our goal is to improve the through-plane resolution of different MRI tissue contrasts and leverage the distinct volumetric appearance in eye organs to generate tissue contrast-specific atlases across populations (Fig. 2). Our proposed framework can be divided into three sections: 1) super-resolution preprocessing, 2) coarse unbiased template

generation, and 3) hierarchical deep probabilistic registration refinement.

A. Super-Resolution Preprocessing

We applied the synthetic multi-orientation resolution enhancement (SMORE) algorithm to generate super-resolution images [9] [32]. The input image for SMORE is an anisotropic volume, modeled with a spatial resolution of $l \times l \times h$, where l and h have units of mm and $h > l$. Here, the images have a high ratio between the in-plane resolution and through-plane resolution ($h/l > 6$). SMORE learns a correspondence between low-resolution (LR) and high-resolution (HR) image patches using only the in-plane slices as training data. The output of SMORE is an isotropic HR image with resolution $l \times l \times l$.

B. Coarse Unbiased Template Generation

Given the enriched context from the super-resolution algorithm in the prior step, we can now use the super-resolution images to create a generalized eye organ representation as a population-wise atlas template. Typically, we perform image registration to align and match the eye anatomy with imaging tools, e.g., ANTs and NiftyReg [33], [34]. However, registration to a single target image with these tools is biased to a single fixed reference template.

To tackle this bias, we apply an unbiased template generation method that results in a coarse, generalized template despite the significant variance in eye morphology. Specifically, for each tissue contrast, we randomly sampled a small set of 25 subjects and generated an average mapping to coarsely align the skull region. The initial template is an average mapping of the 25 subjects, meaning it is unbiased to any of the subjects [35], [36]. We performed hierarchical metric-based registration (consisting of rigid, affine, and then deformable registration) with ANTs to iteratively compute an average mapping in a separate spatial alignment for each tissue contrast. The computed average template in each epoch was the fixed template for the next epoch. We performed the same hierarchical procedure iteratively until the registration loss converged. We leveraged a small population sample to generate a coarse unbiased template due to the required time for loss convergence, which was 3 days for 20 samples and 3.5 weeks for 100 samples using an Intel Xeon W-2255 CPU. We hypothesize that the iterative-generated template can provide the representational anatomy of eye organs with minimal bias.

C. Hierarchical Deep Probabilistic Registration Refinement

We refined the template using the remaining randomly selected samples in addition to the 25 used for the coarse template generation. Our goal is to generalize the anatomical characteristics of eye organs across a large population. We used the VoxelMorph-Probabilistic model to refine the coarse atlas templates [29]. The deep probabilistic network predicts the deformation field modeled as a diffeomorphic transformation, meaning the transformation is smooth and invertible. Additionally, the model is unsupervised and does not require labels. In addition to the probabilistic model, we also compared with the non-probabilistic VoxelMorph-Original [37]. After

TABLE I
OVERVIEW OF FOUR MULTI-CONTRAST MRI DATASET SAMPLES

Tissue Contrast	T1W Pre-Contrast	T1W Post-Contrast	T2W TSE	T2W FLAIR
Anatomical Regions	Optic nerve, recti muscles, globe, orbital fat			
Sample Size	44	100	100	100
In-Plane Resolution (min-max, mm)	0.430-0.938	0.375-0.938	0.391-0.898	0.393-0.898
Slice Thickness (min-max, mm)*	6.00	4.00-6.00	6.00	4.00-6.00

*: This study used fully deidentified data. Information on the slice-selection profiles and use of slice gaps were removed in the deidentification process.

refinement, the resulting atlases serve as reference images in separate spatial alignments for each tissue contrast. After forming the atlas template, we generate labels using majority voting.

IV. EXPERIMENTAL SETUP

To evaluate our proposed unbiased atlas generation framework, we performed experiments to determine the quality of our super-resolution preprocessing and image registration pipeline. We tested our framework using inverse label transfer with four MRI tissue contrasts. We applied the inverse transformation using the deformation field of the atlas label and compared it to the original label for each subject. We computed the Dice score to determine the similarity between the atlas label and the moving image space label.

A. Datasets

We retrieved de-identified volumetric scans in four different MRI tissue contrasts from 1842 patients from ImageVU, a medical image repository from Vanderbilt University Medical Center. We obtained approval from the Institutional Review Board (IRB 131461), and informed consent was waived due to the use of de-identified data. The tissue contrasts were T1-weighted pre-contrast, T1-weighted post-contrast, T2-weighted turbo-spin echo (TSE), and T2-weighted fluid attenuated inversion recovery (FLAIR). The ratio between the through-plane and in-plane resolution varied with a large level of ranges (Table I). Across all four tissue contrasts studied here, the x - y resolution varied from 0.457 mm to 0.635 mm, and the slice thickness varied from 1.23 mm to 7.00 mm. The large values for slice thickness limit our ability to distinguish spatial information. We randomly selected 100 subjects from each tissue contrast to both generate and evaluate the unbiased template, performing quality assurance to make sure the morphological conditions of the eyes are similar (e.g., healthy, no implant artifacts). For T1-weighted pre-contrast, there were only 44 total subjects. The subjects that we sampled for each imaging tissue contrast were different, resulting in different spatial alignments for each tissue contrast. All selected subject scans consisted of four organ ground truth labels: 1) optic nerve, 2) recti muscles, 3) globe and 4) orbital fat.

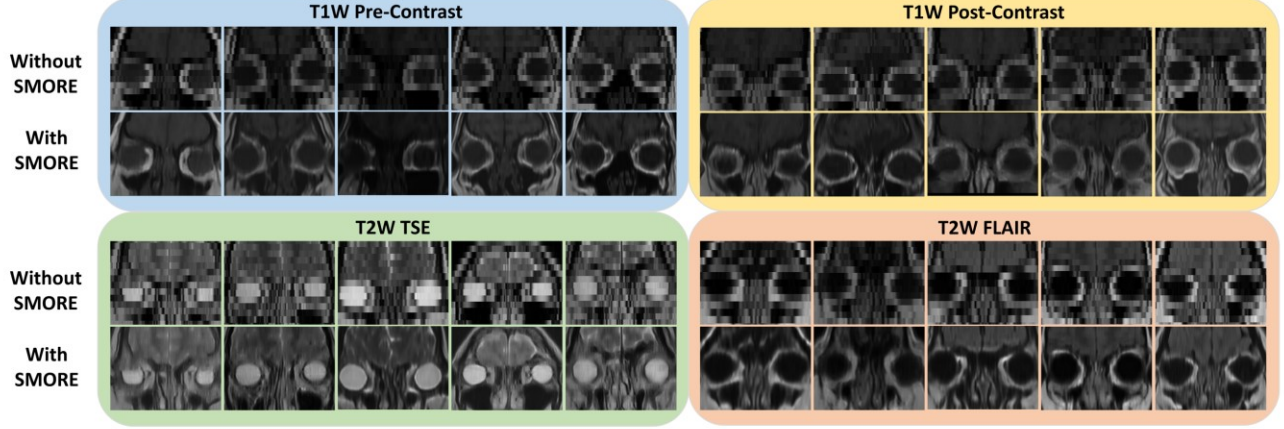


Fig. 3. By applying SMORE (bottom rows), the anatomical context of the eye region is distinctly shown in the coronal view with a clear improvement in resolution across five unpaired patients in each tissue contrast compared to images without SMORE applied (top rows).

B. Implementation Setup

1) *Super-Resolution Preprocessing*: We apply the SMORE super-resolution algorithm to generate upsampled MRIs. After applying SMORE, we resampled the isotropic resolution to $0.8 \text{ mm} \times 0.8 \text{ mm} \times 0.8 \text{ mm}$ using cubic interpolation. We further cropped and padded the MRI volumes to $256 \times 256 \times 224$ voxels.

2) *Coarse Unbiased Template Generation*: To generate the coarse unbiased template, we performed a conventional metric-based registration algorithm with the ANTs toolkit. We leveraged the multivariate template construction tool, which generates an average template that is not biased to a single subject. We applied both rigid and affine registration to align the anatomical locations of the head skull and eye organs, followed by SyN registration, which is a deformable registration algorithm with the similarity metric of cross-correlation. We chose four resolution levels (6, 4, 2, and 1) and iterated over each level for 100, 100, 70, and 20 iterations, respectively. We performed this registration process for six epochs and selected the generated template for each tissue contrast after the registration losses converged.

3) *Hierarchical Registration Refinement*: We used the remaining samples to refine the coarse template and generate a

refined atlas template. As VoxelMorph-Original and VoxelMorph-Probabilistic assume the images only have non-linear spatial misalignment, we used the same hyperparameters in the template generation step to perform metric-based affine registration for the remaining samples as an initial registration alignment. Both the resolution and volumetric dimension of the MRI scans remained the same in the template generation stage (resolution: $0.8 \text{ mm} \times 0.8 \text{ mm} \times 0.8 \text{ mm}$, dimension: $256 \times 256 \times 224$ voxels). We then trained the deep probabilistic framework available from VoxelMorph-Probabilistic and the non-probabilistic VoxelMorph-Original model for comparison. Due to hardware limitations, the batch size was 1. We used the Adam optimizer with a learning rate of 10^{-4} [38]. After the deep probabilistic refinement, we have a separate unbiased atlas for each tissue contrast.

V. RESULTS AND DISCUSSION

A. Qualitative Comparison With and Without Super-Resolution Preprocessing

The super-resolution preprocessing enhanced the through-plane resolution images for each tissue contrast, with more distinctive appearances in eye organs (Fig. 3). The boundaries across tissues and anatomies are substantially clearer. This

TABLE II
QUANTITATIVE EVALUATION OF INVERSE TRANSFERRED LABEL FOR MULTIPLE EYE ORGANS ACROSS ALL PATIENTS

Tissue Contrast	First Stage	Second Stage	Optic Nerve Dice Score	Recti Muscles Dice Score	Globe Dice Score	Orbital Fat Dice Score	Average Dice Score
T1W Pre-Contrast	ANTs	×	0.586±0.0532	0.634±0.0339	0.904±0.0253	0.782±0.0362	0.727±0.132
	ANTs	VoxelMorph-Original	0.635±0.0420	0.687±0.0420	0.920±0.0274	0.790±0.0343	0.758±0.140
	ANTs	VoxelMorph-Probabilistic	0.651±0.0358	0.712±0.0301	0.931±0.0227	0.810±0.0319	0.776±0.115*
T1W Post-Contrast	ANTs	×	0.601±0.0478	0.628±0.0357	0.901±0.0244	0.765±0.0344	0.724±0.129
	ANTs	VoxelMorph-Original	0.647±0.0401	0.679±0.0365	0.922±0.0241	0.801±0.0255	0.762±0.124
	ANTs	VoxelMorph-Probabilistic	0.688±0.0310	0.691±0.0295	0.935±0.0210	0.815±0.0224	0.782±0.107*
T2W TSE	ANTs	×	0.624±0.0435	0.630±0.0348	0.899±0.0257	0.771±0.0312	0.731±0.143
	ANTs	VoxelMorph-Original	0.651±0.0387	0.652±0.0310	0.905±0.0261	0.780±0.0331	0.747±0.141
	ANTs	VoxelMorph-Probabilistic	0.660±0.0365	0.687±0.0288	0.917±0.0303	0.799±0.0267	0.766±0.119*
T2W FLAIR	ANTs	×	0.654±0.0353	0.586±0.0314	0.911±0.0201	0.824±0.0259	0.744±0.141
	ANTs	VoxelMorph-Original	0.660±0.0320	0.601±0.0320	0.915±0.0223	0.837±0.0219	0.753±0.143
	ANTs	VoxelMorph-Probabilistic	0.679±0.0285	0.634±0.0267	0.923±0.0189	0.834±0.0201	0.768±0.110*

*: $p < 0.001$ using the Wilcoxon signed-rank test.

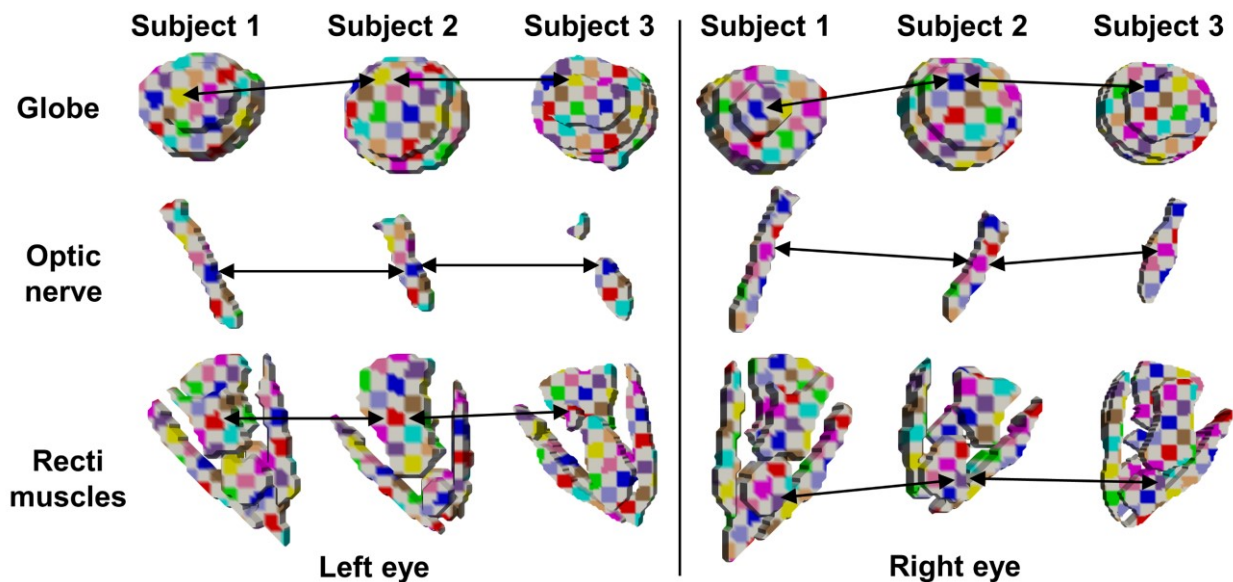


Fig. 4. The atlas is generalizable across the variation in subjects, demonstrated by consistent registration for several subjects. The checkerboard shows the inverse deformation from atlas labels to moving subject labels for several subjects from the T2-weighted FLAIR tissue contrast. The arrows track a single square across subjects.

increase in image quality also demonstrates the distinctive variability of the eye organs across the population.

B. Registration Comparisons Across Multi-Contrast Imaging

After we performed super-resolution preprocessing on all imaging cohorts, we performed hierarchical registration to align the anatomy from moving imaging samples to the unbiased atlas template. We applied ANTs as the first stage with a metric-based registration algorithm to create a baseline result across the four different tissue contrasts.

We performed the second stage registration using VoxelMorph-Original and VoxelMorph-Probabilistic (Table II). We observed a statistically significant improvement in the Dice score across the four tissue contrasts using the Wilcoxon signed-rank test. With the deep probabilistic model as the second stage, the label transfer performance significantly improved across all tissue contrasts. The registration was consistent across the variable subjects (Fig. 4).

We observe that the unclear boundaries in the atlases brought by the low resolution in through-plane axis are minimized by applying SMORE (Fig. 5). The mapping more clearly shows the anatomy of the eye organs and generalized population characteristics, with limited deformation in the eye organ region.

C. Discussion

We presented a complete framework to adapt a large population of multi-contrast imaging for unbiased eye atlas generation. We integrated both metric-based and deep learning-based registration as a coarse-to-fine framework to refine the transfer process of eye organ anatomy across populations. By applying SMORE as the first step in the framework, the SMORE model learned the high-resolution context from the in-plane axial slice and applied the correspondence to restore the

refined details for the through-plane coronal and sagittal slices. With the restored high-resolution details, the unbiased average templates generated demonstrate a substantial enhancement in both organ appearance and boundaries for each tissue contrast. The restored high-resolution details provide a clearer appearance to guide the registration process, especially the skull region. With the rigid, affine, and deformable registration from ANTs, moving subject scans demonstrate coarse alignment with respect to the eye organs. The initial template is an average mapping that is not biased to a single subject, and each tissue contrast has a separate geometry. We further refined the intermediate registered output with a deep learning-based approach to generate a larger deformation field for anatomy alignment. Moreover, we integrated probabilistic neural networks to smooth the generated deformation field and to adapt diffeomorphism for registration, which enhanced the anatomical context transfer performance across all tissue contrasts.

Since the coarse template generation relies on an average mapping across 25 subjects, the atlases generated here are unbiased to a particular subject. This unbiased mapping addresses the limited information generalizable to a population from single subject atlases such as the Talairach-Tournoux human brain atlas [39]. There are several potential uses for these eye atlases. In medical research, they could be used to quantitatively measure eye shape across a variable population, similar to how brain atlases can allow for a standardized reference to quantify the volume of brain structures or size of small lesions. Atlases also allow for automatic labeling of structures of interest, providing confidence in images with poor quality [40]. Due to the application of the super-resolution algorithm, the eye atlases restore high resolution details that are not available in scans with a large slice thickness, meaning they provide a high-resolution reference for images with poor through-plane quality. Clinically, these atlases could be useful

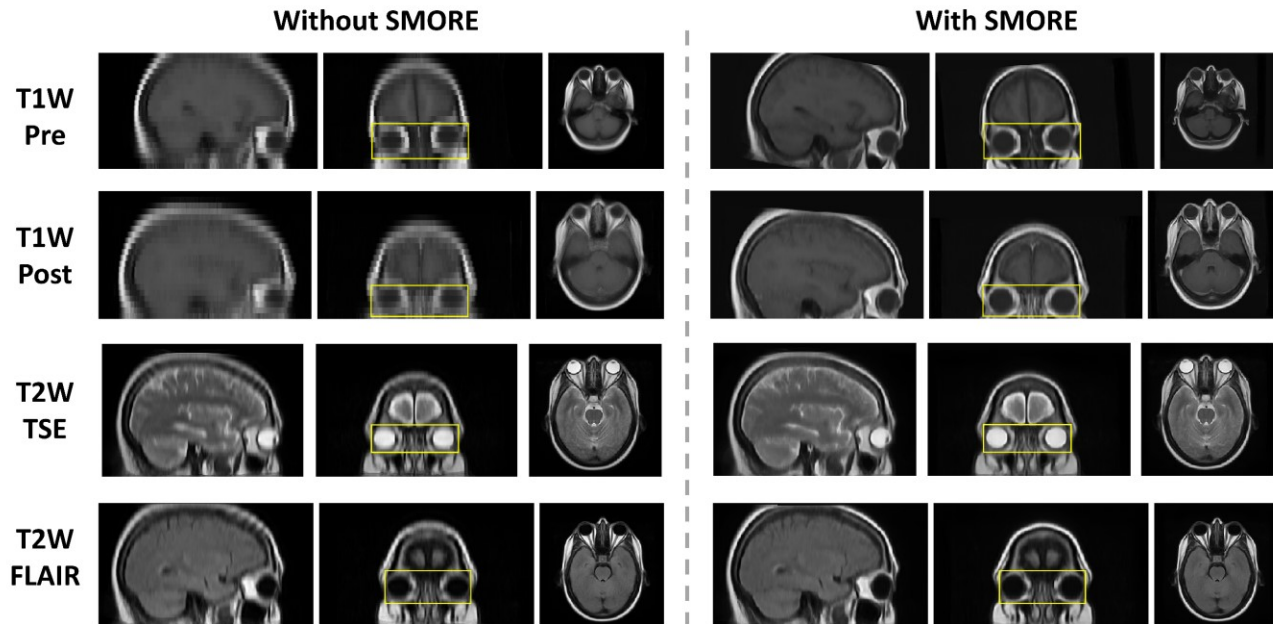


Fig. 5. When using SMORE to generate an unbiased eye atlas, the anatomical context from eye organs to brain is refined, and tissues are clearly distinguishable compared to the unbiased eye atlas without using SMORE. The eye organ region (yellow bounding box) shows little deformation.

for surgical planning, targeting and training, common applications of brain atlases [41]. The atlas generation pipeline also does not rely on any specific MRI tissue contrast, allowing for a consistent method for generating atlases across a broad range of tissue contrasts.

Although the generated unbiased templates for each tissue contrast demonstrate the distinctive appearance of the eye organs across population, multiple bottlenecks and limitations exist in the proposed framework. The first bottleneck is to generate a coarse unbiased template with ANTs. We only leveraged a small portion (25 subjects) of the imaging cohort to generate the initial average template. The main limitation of applying ANTs is the low computational efficiency, taking several days to generate a coarse template with only a small portion of samples, which can be a bottleneck without access to computing cluster resources. Therefore, an end-to-end approach to generate a coarse unbiased template is desirable. Another computational constraint is the hierarchical registration framework. Before applying deep learning-based registration algorithms like VoxelMorph-Original and VoxelMorph-Probabilistic, all imaging samples must be affine registered. However, limited studies have proposed adapting a deep learning network that can perform affine and deformable registration in parallel to avoid this sequential processing. Researchers have introduced multi-task networks combining affine and deformable registration to enhance the effectiveness and the computational efficiency of registration algorithms, but these networks have not shown substantial improvement over VoxelMorph-Original without the use of additional registration algorithms like Demons [42]. Another limitation of this framework is that the resulting atlases are not in registration, meaning we have a separate spatial geometry for each tissue contrast.

The framework presented here allows for the creation of a reference coordinate system for the eye. Given the substantial variation in eye morphology, the eye atlases could be useful for comparing anatomy across a population. With the atlases created here, we have a means for exploring quantitative geometric measurements of eye shape despite systematic differences within a population.

VI. CONCLUSION

In summary, we introduced a framework to generate unbiased eye atlases across a large population using images with anisotropic voxels. We applied a deep learning super-resolution algorithm to learn the high-resolution characteristics from axial slices and applied this high-resolution correspondence to the coronal and sagittal slices. We adapted the restored high-resolution context to generate an unbiased eye atlas with a separate spatial geometry for each tissue contrast, using hierarchical registration with an average mapping to avoid biasing the atlas by registering to a single target. We integrated a deep probabilistic network to enhance the smoothness of the deformation field and increase registration performance with diffeomorphism. The generated average template from each tissue contrast illustrates the distinctive appearance of eye organs and generalizes across a large population cohort with significant improvement in anatomical label transfer performance compared to metric-based registration alone.

REFERENCES

- [1] B. Tan *et al.*, “Ultrawide field, distortion-corrected ocular shape estimation with MHz optical coherence tomography (OCT),”

- Biomed Opt Express*, vol. 12, no. 9, p. 5770, Sep. 2021, doi: 10.1364/BOE.428430.
- [2] L. S. Lim *et al.*, “MRI of posterior eye shape and its associations with myopia and ethnicity,” *British Journal of Ophthalmology*, Dec. 2019, doi: 10.1136/bjophthalmol-2019-315020.
- [3] R. Aseem *et al.*, “Positional Variation of the Infraorbital Foramen in Caucasians and Black Africans from Britain: Surgical Relevance and Comparison to the Existing Literature,” *Journal of Craniofacial Surgery*, vol. 32, no. 3, pp. 1162–1165, May 2021, doi: 10.1097/SCS.00000000000007014.
- [4] D. Dean *et al.*, “Average African American Three-Dimensional Computed Tomography Skull Images,” *Journal of Craniofacial Surgery*, vol. 9, no. 4, pp. 348–358, Jul. 1998, doi: 10.1097/00001665-199807000-00011.
- [5] D. H. Kim, J.-S. Jun, and R. Kim, “Ultrasonographic measurement of the optic nerve sheath diameter and its association with eyeball transverse diameter in 585 healthy volunteers,” *Sci Rep*, vol. 7, no. 1, p. 15906, Nov. 2017, doi: 10.1038/s41598-017-16173-z.
- [6] M. Vaiman, R. Abuita, and I. Bekerman, “Optic nerve sheath diameters in healthy adults measured by computer tomography,” *Int J Ophthalmol*, vol. 8, no. 6, pp. 1240–1244, Dec. 2015.
- [7] D. A. Atchison *et al.*, “Eye Shape in Emmetropia and Myopia,” *Investigative Ophthalmology & Visual Science*, vol. 45, no. 10, p. 3380, Oct. 2004, doi: 10.1167/iovs.04-0292.
- [8] I. Bekerman, P. Gottlieb, and M. Vaiman, “Variations in Eyeball Diameters of the Healthy Adults,” *J Ophthalmol*, vol. 2014, pp. 1–5, 2014, doi: 10.1155/2014/503645.
- [9] C. Zhao, B. E. Dewey, D. L. Pham, P. A. Calabresi, D. S. Reich, and J. L. Prince, “SMORE: A Self-Supervised Anti-Aliasing and Super-Resolution Algorithm for MRI Using Deep Learning,” *IEEE Trans Med Imaging*, vol. 40, no. 3, pp. 805–817, Mar. 2021, doi: 10.1109/TMI.2020.3037187.
- [10] S. Jain *et al.*, “Advances and prospects for the Human BioMolecular Atlas Program (HuBMAP),” *Nat Cell Biol*, Jul. 2023, doi: 10.1038/s41556-023-01194-w.
- [11] X. Wang, R. Zhang, C. Shen, T. Kong, and L. Li, “Dense Contrastive Learning for Self-Supervised Visual Pre-Training,” in *2021 IEEE/CVF Conference on Computer Vision and Pattern Recognition (CVPR)*, IEEE, Jun. 2021, pp. 3023–3032. doi: 10.1109/CVPR46437.2021.00304.
- [12] P. Lorenzen, M. Prastawa, B. Davis, G. Gerig, E. Bullitt, and S. Joshi, “Multi-modal image set registration and atlas formation,” *Med Image Anal*, vol. 10, no. 3, pp. 440–451, Jun. 2006, doi: 10.1016/J.MEDIA.2005.03.002.
- [13] N. Kovačević *et al.*, “A Three-dimensional MRI Atlas of the Mouse Brain with Estimates of the Average and Variability,” *Cerebral Cortex*, vol. 15, no. 5, pp. 639–645, May 2005, doi: 10.1093/cercor/bhh165.
- [14] Q. Wang *et al.*, “The Allen Mouse Brain Common Coordinate Framework: A 3D Reference Atlas,” *Cell*, vol. 181, no. 4, pp. 936–953.e20, May 2020, doi: 10.1016/J.CELL.2020.04.007.
- [15] F. Shi *et al.*, “Infant Brain Atlases from Neonates to 1- and 2-Year-Olds,” *PLoS One*, vol. 6, no. 4, p. e18746, Apr. 2011, doi: 10.1371/journal.pone.0018746.
- [16] M. Kuklisova-Murgasova *et al.*, “A dynamic 4D probabilistic atlas of the developing brain,” *Neuroimage*, vol. 54, no. 4, pp. 2750–2763, Feb. 2011, doi: 10.1016/J.NEUROIMAGE.2010.10.019.
- [17] A. Gholipour *et al.*, “A normative spatiotemporal MRI atlas of the fetal brain for automatic segmentation and analysis of early brain growth,” *Sci Rep*, vol. 7, no. 1, p. 476, Mar. 2017, doi: 10.1038/s41598-017-00525-w.
- [18] Y. Zhang, F. Shi, G. Wu, L. Wang, P.-T. Yap, and D. Shen, “Consistent Spatial-Temporal Longitudinal Atlas Construction for Developing Infant Brains,” *IEEE Trans Med Imaging*, vol. 35, no. 12, pp. 2568–2577, Dec. 2016, doi: 10.1109/TMI.2016.2587628.
- [19] D. Rajashekar *et al.*, “High-resolution T2-FLAIR and non-contrast CT brain atlas of the elderly,” *Sci Data*, vol. 7, no. 1, p. 56, Feb. 2020, doi: 10.1038/s41597-020-0379-9.
- [20] H. H. Lee *et al.*, “Construction of a multi-phase contrast computed tomography kidney atlas,” in *Medical Imaging 2021: Image Processing*, B. A. Landman and I. Išgum, Eds., SPIE, Feb. 2021, p. 61. doi: 10.1117/12.2580561.
- [21] H. H. Lee *et al.*, “Multi-contrast computed tomography healthy kidney atlas,” *Comput Biol Med*, vol. 146, p. 105555, Jul. 2022, doi: 10.1016/J.COMPBIOMED.2022.105555.
- [22] H. H. Lee *et al.*, “Supervised deep generation of high-resolution arterial phase computed tomography kidney substructure atlas,” in *Medical Imaging 2022: Image Processing*, I. Išgum and O. Colliot, Eds., SPIE, Apr. 2022, p. 97. doi: 10.1117/12.2608290.
- [23] J. Ashburner, “A fast diffeomorphic image registration algorithm,” *Neuroimage*, vol. 38, no. 1, pp. 95–113, Oct. 2007, doi: 10.1016/J.NEUROIMAGE.2007.07.007.

- [24] B. B. Avants, C. L. Epstein, M. Grossman, and J. C. Gee, "Symmetric diffeomorphic image registration with cross-correlation: Evaluating automated labeling of elderly and neurodegenerative brain," *Med Image Anal*, vol. 12, no. 1, pp. 26–41, Feb. 2008, doi: 10.1016/J.MEDIA.2007.06.004.
- [25] G. Balakrishnan, A. Zhao, M. R. Sabuncu, A. V. Dalca, and J. Guttag, "An Unsupervised Learning Model for Deformable Medical Image Registration," in *2018 IEEE/CVF Conference on Computer Vision and Pattern Recognition*, IEEE, Jun. 2018, pp. 9252–9260. doi: 10.1109/CVPR.2018.00964.
- [26] A. V. Dalca, A. Bobu, N. S. Rost, and P. Golland, "Patch-Based Discrete Registration of Clinical Brain Images," pp. 60–67, 2016, doi: 10.1007/978-3-319-47118-1_8.
- [27] D. Rueckert, L. I. Sonoda, C. Hayes, D. L. G. Hill, M. O. Leach, and D. J. Hawkes, "Nonrigid registration using free-form deformations: application to breast MR images," *IEEE Trans Med Imaging*, vol. 18, no. 8, pp. 712–721, 1999, doi: 10.1109/42.796284.
- [28] T. Vercauteren, X. Pennec, A. Perchant, and N. Ayache, "Diffeomorphic demons: Efficient non-parametric image registration," *Neuroimage*, vol. 45, no. 1, pp. S61–S72, Mar. 2009, doi: 10.1016/J.NEUROIMAGE.2008.10.040.
- [29] A. V. Dalca, G. Balakrishnan, J. Guttag, and M. R. Sabuncu, "Unsupervised learning of probabilistic diffeomorphic registration for images and surfaces," *Med Image Anal*, vol. 57, pp. 226–236, Oct. 2019, doi: 10.1016/J.MEDIA.2019.07.006.
- [30] S. Zhao, Y. Dong, E. Chang, and Y. Xu, "Recursive Cascaded Networks for Unsupervised Medical Image Registration," in *2019 IEEE/CVF International Conference on Computer Vision (ICCV)*, IEEE, Oct. 2019, pp. 10599–10609. doi: 10.1109/ICCV.2019.01070.
- [31] S. di Yang *et al.*, "Target organ non-rigid registration on abdominal CT images via deep-learning based detection," *Biomed Signal Process Control*, vol. 70, p. 102976, Sep. 2021, doi: 10.1016/J.BSPC.2021.102976.
- [32] S. W. Remedios *et al.*, "Self-Supervised Super-Resolution for Anisotropic MR Images with and Without Slice Gap," pp. 118–128, 2023, doi: 10.1007/978-3-031-44689-4_12.
- [33] B. B. Avants, N. J. Tustison, M. Stauffer, G. Song, B. Wu, and J. C. Gee, "The Insight ToolKit image registration framework," *Front Neuroinform*, vol. 8, Apr. 2014, doi: 10.3389/fninf.2014.00044.
- [34] M. Modat, D. M. Cash, P. Daga, G. P. Winston, J. S. Duncan, and S. Ourselin, "Global image registration using a symmetric block-matching approach," *Journal of Medical Imaging*, vol. 1, no. 2, p. 024003, Sep. 2014, doi: 10.1117/1.JMI.1.2.024003.
- [35] B. B. Avants *et al.*, "The Optimal Template Effect in Hippocampus Studies of Diseased Populations," *Neuroimage*, vol. 49, no. 3, p. 2457, Feb. 2010, doi: 10.1016/J.NEUROIMAGE.2009.09.062.
- [36] B. B. Avants, N. J. Tustison, G. Song, P. A. Cook, A. Klein, and J. C. Gee, "A Reproducible Evaluation of ANTs Similarity Metric Performance in Brain Image Registration," *Neuroimage*, vol. 54, no. 3, p. 2033, Feb. 2011, doi: 10.1016/J.NEUROIMAGE.2010.09.025.
- [37] G. Balakrishnan, A. Zhao, M. R. Sabuncu, J. Guttag, and A. V. Dalca, "VoxelMorph: A Learning Framework for Deformable Medical Image Registration," *IEEE Trans Med Imaging*, vol. 38, no. 8, pp. 1788–1800, Aug. 2019, doi: 10.1109/TMI.2019.2897538.
- [38] D. P. Kingma and J. Ba, "Adam: A Method for Stochastic Optimization," in *3rd International Conference for Learning Representations*, Dec. 2014. Accessed: Sep. 24, 2023. [Online]. Available: <http://arxiv.org/abs/1412.6980>
- [39] D. A. Dickie *et al.*, "Whole Brain Magnetic Resonance Image Atlases: A Systematic Review of Existing Atlases and Caveats for Use in Population Imaging," *Front Neuroinform*, vol. 11, Jan. 2017, doi: 10.3389/fninf.2017.00001.
- [40] W. L. Nowinski, "Usefulness of brain atlases in neuroradiology: Current status and future potential," *Neuroradiol J*, vol. 29, no. 4, p. 260, Aug. 2016, doi: 10.1177/1971400916648338.
- [41] W. L. Nowinski, "Evolution of Human Brain Atlases in Terms of Content, Applications, Functionality, and Availability," *Neuroinformatics*, vol. 19, no. 1, pp. 1–22, Jan. 2021, doi: 10.1007/s12021-020-09481-9.
- [42] X. Gao, J. Van Houtte, Z. Chen, and G. Zheng, "DeepASDM: a Deep Learning Framework for Affine and Deformable Image Registration Incorporating a Statistical Deformation Model," in *2021 IEEE EMBS International Conference on Biomedical and Health Informatics (BHI)*, IEEE, Jul. 2021, pp. 1–4. doi: 10.1109/BHI50953.2021.9508553.